


Article

Fabrication of Vitrified Bond Diamond Grinding Wheel via LCD Photopolymerization

Zhaoqi Chen ¹, Na Xiao ², Ping Han ^{1,*} , Zhao Wang ³ and Guoju Bai ¹

¹ School of Materials Science and Engineering, Henan University of Technology, Zhengzhou 450001, China; 17698050650@163.com (Z.C.); bgj15630603152@163.com (G.B.)

² Faculty of Engineering, Huanghe University of Science and Technology, Zhengzhou 450007, China; xiaona201608156@163.com

³ Beijing Gangyan Diamond Products Company, Beijing 102200, China; wangzhao@gangyan-diamond.com

* Correspondence: hanping02712@163.com

Abstract: In this paper, a liquid crystal display (LCD) photopolymerization method is proposed, and a vitrified bond diamond grinding wheel is successfully prepared. A high-performance vitrified bond was obtained by melting SiO₂-B₂O₃-Al₂O₃-Na₂O ceramic raw materials and used for grinding wheel preparation. LCD photopolymerization technology is characterized by high precision in shaping, fast processing speed, and superior quality, making it a promising technology for fabricating vitrified bond diamond grinding wheels. The preparation of vitrified bond slurry with high solid content and low viscosity was extensively investigated to meet the fabrication requirements. The effects of dispersant, the particle size of the vitrified bond, and solid content on the viscosity of the slurry were systematically analyzed. The vitrified bond slurry with solid content up to 65 wt.% (approximately 45.5 vol.%) was successfully prepared and met the requirements for printing. Furthermore, we explored the optimal formulation of the grinding wheel, debinding and sintering conditions, sintering temperature, grit-to-bond ratio, and the evaluation of the grinding performance of the wheel on hard and brittle materials, such as silicon carbide ceramic. Vitrified bond and abrasive slurry systems with a solid content of 65 wt.% (approximately 42.8 vol.%) were prepared. The results show that the vitrified bond diamond grinding wheel exhibits optimal comprehensive performance, with a sintering temperature of 680 °C and a grit-to-bond ratio of 4:6. The minimum surface roughness of the workpiece after grinding was 1.767 μm, the material removal rate was 5.08 mg/s, the grinding ratio was 9.78, and the friction coefficient was stabilized at about 0.5 during grinding. This paper guides the manufacturing of vitrified bond diamond grinding wheels via LCD photopolymerization.

Keywords: vitrified bond; grinding wheel; liquid crystal display; photopolymerization; mechanical property; grinding performance



Citation: Chen, Z.; Xiao, N.; Han, P.; Wang, Z.; Bai, G. Fabrication of Vitrified Bond Diamond Grinding Wheel via LCD Photopolymerization. *Coatings* **2023**, *13*, 2079. <https://doi.org/10.3390/coatings13122079>

Academic Editors: Majid Tolouei-Rad, Muhammad Aamir and Riaz Muhammad

Received: 27 October 2023
Revised: 2 December 2023
Accepted: 11 December 2023
Published: 13 December 2023



Copyright: © 2023 by the authors. Licensee MDPI, Basel, Switzerland. This article is an open access article distributed under the terms and conditions of the Creative Commons Attribution (CC BY) license (<https://creativecommons.org/licenses/by/4.0/>).

1. Introduction

Vitrified bond diamond grinding wheels are widely used in cemented carbide [1], semiconductor finishing [2], and hard, brittle materials because of their good heat resistance, high grinding accuracy, good self-sharpening, and long dressing interval, and their use is increasing year by year [3,4]. Low-temperature vitrified bonds are typically obtained by melting oxides at elevated temperatures and quenching them in deionized water. The performance of vitrified bond diamond wheels relies heavily on the properties of the vitrified bond [5]. While there have been numerous investigations on bond characteristics, such as nanosizing of vitrified bonds [6,7], microcrystalline vitrification [8], and the use of various additives [9,10], there has been a lack of research concerning the role of B₂O₃ content. B₂O₃ possesses a low melting temperature of only 450 °C, and its incorporation into the vitrified bond significantly reduces the sintering temperature [11], offering the potential for ultra-low-temperature sintering of vitrified bond diamond wheels. We extensively

investigated the $\text{SiO}_2\text{-B}_2\text{O}_3\text{-Al}_2\text{O}_3\text{-Na}_2\text{O}$ system with varying B_2O_3 content in the vitrified bond to explore this possibility. The results show that when the mole fraction of B_2O_3 is 15%, a high-performance vitrified bond can be formed. The refractoriness of the vitrified bond is $740\text{ }^\circ\text{C}$, and the thermal expansion coefficient is 5.62×10^{-6} . The fluidity of the vitrified bond sintered at $680\text{ }^\circ\text{C}$ for 2 h is 120%. Hence, this vitrified bond system serves as the foundation for an in-depth study in this paper.

The conventional method for preparing vitrified bond diamond grinding wheels involves cold pressing using steel molds [12]. In this process, diamond abrasives and vitrified bonds are weighed in specific proportions, and a temporary adhesive like dextrin powder or polyvinyl alcohol is utilized to bind the mixture. The resulting mixture is then injected into molds and cold-pressed [13]. However, this approach has limitations in manufacturing complex-shaped grinding wheels due to the dependency on molds. To address this challenge and enable the creation of highly designable and individualized grinding wheel shapes, additive manufacturing (3D printing) combined with CAD drawing technology has emerged [14,15]. This approach offers the possibility of producing complex structures without molding, reducing long production cycles. Thus, 3D-printing technologies applied in diamond tool applications primarily include selective laser sintering (SLS) [16], selective laser melting (SLM) [17,18], direct ink writing (DIW) [19], and photopolymerization-based methods (stereolithography, SLA, and digital light processing, DLP) [20,21]. Among these techniques, laser sintering methods are mainly used for metal-bond diamond tools. Yang et al. [16] utilized SLS technology to manufacture metal-bond diamond grinding wheels with controlled diamond distribution. Li et al. [17,18] employed AlSi10Mg as a bond and used SLM technology to fabricate porous structured metal-bond diamond grinding wheels. Huang et al. [19] used DIW technology to create vitrified bond diamond grinding wheels with complex pore shapes, including solid, triangular, and lattice structures. Guo et al. [20,21] developed a diamond grinding plate using UV-curable resin as the bond. Furthermore, by integrating traditional preparation techniques with 3D-printing technology, Lin et al. [22] successfully fabricated vitrified bond diamond grinding wheels using 3D-printed molds and gel-casting technology.

The low cost and high precision of SLA and DLP technologies have garnered considerable attention from researchers [23,24]. The key to these technologies lies in preparing high solid content and low-viscosity slurry. Griffith et al. [25,26] was among the first to propose applying SLA technology in ceramic fabrication. Their research revealed that a low solid content in the slurry could lead to printing defects, breakage, or even failure. Conversely, increasing the solid content of the slurry led to a gradual rise in viscosity, notably when the solid content exceeded 30 vol.%. Thickness exhibited an exponential increase with higher solid content. As a result, extensive research has been conducted to increase solid content while reducing viscosity. Adake et al. [27] effectively utilized oleic acid and stearic acid as dispersants to modify aluminum oxide powder, yielding a ceramic slurry with a solid content of 40 vol.%. This demonstrated that appropriate carboxylic acids can effectively reduce slurry viscosity. Zhang et al. [28] modified alumina powder with dicarboxylic acid as a dispersant to prepare a ceramic slurry with a solid content of 45 vol.% and successfully designed alumina ceramics with a density of up to 96.5%. They achieved printing of highly dense alumina ceramics with a thickness of up to 96.5%. Compared with SLA and DLP, liquid crystal display (LCD) photopolymerization technology [29–32] uses a series of UV LCD light sources, and the light source is directly irradiated to the construction area in a parallel manner. This light will not expand, and there is no pixel distortion. It can achieve higher resolution and smaller pixel size printing and can almost entirely restore the model.

LCD photopolymerization technology has been exclusively applied to resin-bonded diamond tools, and no research has been published on vitrified-bonded diamond tools. To address this research gap, this study proposes an LCD photopolymerization 3D-printing method for successfully fabricating vitrified bond diamond grinding wheels. This investigation systematically explores the effects of dispersants, bond particle size, and solid content on slurry viscosity to achieve a high solid content and low-viscosity slurry. Furthermore,

this study evaluates the optimal formulation for the grinding wheels, including debinding and sintering regimes, sintering temperature, grit-to-bond ratio, and the grinding performance of the wheels when grinding brittle materials such as silicon carbide.

2. Experimental

2.1. Material

The raw materials used in this experiment were SiO_2 , H_3BO_3 , Al_2O_3 , and Na_2CO_3 , all of which were analytically pure with a purity of 99.8% and obtained from Xilong Science Co., Shantou, China; 1,6-Hexanediol diacrylate (HDDA, $\text{CH}_2=\text{CHCOO}(\text{CH}_2)_6\text{OOCCH}=\text{CH}_2$, 1.01 g/cm^3) was utilized as a diluent; 1,1,1-trimethylolpropane triacrylate (TMPTA, $\text{CH}_2=\text{CHCOOCH}_2)_3\text{-CCH}_2\text{CH}_3$, 1.1 g/cm^3) served as a photosensitive resin monomer; and diphenyl (2,4,6-trimethylbenzoyl) phosphine oxide (TPO, 1.17 g/cm^3) was used as a photoinitiator. Dispersants used in the experiment included polyethylene glycol (PEG), with molecular weights of 200, 400, 800, 1000, and 2000, oleic acid (OA), stearic acid (SA), sodium stearate (SS), and sodium citrate (SC), all purchased from Shanghai Aladdin Bio-Chem Technology Co., Ltd., Shanghai, China, Diamond ($d_{50} = 10 \mu\text{m}$, purity $\geq 99.7\%$, 3.52 g/cm^3 , Yellow River Cyclone Co., Ltd., Zhengzhou, China) was used as abrasive, and white corundum ($d_{50} = 7 \mu\text{m}$, purity $\geq 99\%$, 3.96 g/cm^3 , Zhengzhou Yufa Abrasive Co., Ltd., Zhengzhou, China) was used as auxiliary abrasive. Anhydrous ethanol (analytical grade) was procured from Tianjin KeMio Chemical Reagent Co., Ltd., Tianjin, China.

2.2. Vitrified Bond Preparation

Table 1 presents the molar fraction formulation of the vitrified bond used in the experimental design, which was then converted into mass fraction ratios, as shown in Table 2. To ensure thorough mixing, the raw materials underwent ball milling for 4 h using zirconia balls in a vacuum ball mill (XQM-4, Changsha Tianchuang Powder Technology Co., Ltd., Changsha, China). The resulting mixed powder was placed in a corundum crucible and melted at $1400 \text{ }^\circ\text{C}$ for 2 h. Following this, it was quenched in deionized water and dried at $80 \text{ }^\circ\text{C}$ in an electric blast drying oven for 8 h to obtain the pristine glass precursor. Subsequently, the glass precursor was put into a ball mill with a ball-to-powder ratio of 2:1 and a graded distribution of large, medium, and small balls in a proportion of 2:4:1. The ball mill operated at a speed of 450 r/min for 1 h, 2 h, 4 h, and 6 h, respectively, resulting in vitrified bond with different particle sizes, as illustrated in Figure 1a.

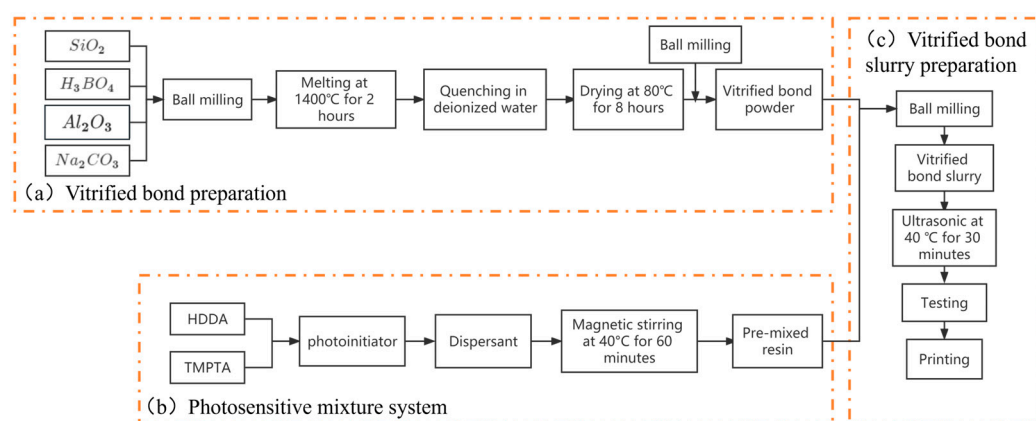


Figure 1. Vitrified bond slurry preparation flowchart.

Table 1. Molar fraction of raw materials for vitrified bond.

Material	SiO_2	B_2O_3	Al_2O_3	Na_2O
	60	15	5	20

Table 2. Mass fraction of raw materials for vitrified bond.

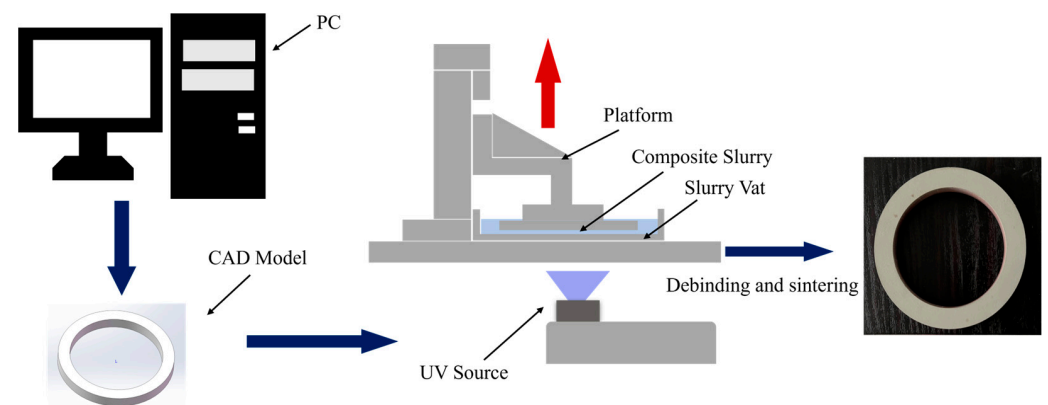
Material	SiO ₂	H ₃ BO ₃	Al ₂ O ₃	Na ₂ CO ₃
	44.57	22.93	6.30	26.20

2.3. Vitrified Bond Slurry Preparation

The solid dispersant was dissolved in ethanol using magnetic stirring in a water bath at 40 °C. A pure vitrified bond slurry with a solid content of 40 wt.% was prepared to explore the optimal slurry system. Firstly, HDDA and TMPTA were mixed in a specific ratio (based on extensive experiments, an HDDA-to-TMPTA ratio of 67:33 was found to ensure the desired molding quality and minimize the mixture's viscosity) through magnetic stirring for 30 min. To fully cure, five wt.% TPO photoinitiator was added to the mix relative to the resin content [33]. Subsequently, dispersants, including PEG (with molecular weights of 200, 400, 800, 1000, and 2000), OA, SA, SS, and SC, were added to the mixture, followed by magnetic stirring for 60 min to obtain a photosensitive mixed system, as shown in Figure 1b. Finally, the mixture was combined with the vitrified bond powder and ball-milled in a vacuum ball mill at 300 r/min for 2 h. Afterward, bubble elimination was carried out using ultrasound at 40 °C for 30 min to remove bubbles from the vitrified bond slurry, resulting in a well-dispersed photosensitive vitrified bond slurry with different viscosities, as illustrated in Figure 1c. Once the optimal slurry system was determined, the abrasive could be added according to the same method, and the slurry system composed of vitrified bond and abrasive could be configured.

2.4. Vitrified Bond Diamond Grinding Wheel Preparation

The photocuring printer is JG MAKER G5 (Shenzhen Aurora Technology Co., Ltd., Shenzhen, China). The printer can emit a laser light source of 405 nm, consistent with the photoinitiator TPO's absorption wavelength. The technology used is LCD photopolymerization with a resolution of 3840 × 2400 (4K). Pour the slurry into the material tank and use SolidWorks 2022 SP0 software to establish a three-dimensional model. Table 3 shows the CAD parameters of the grinding wheel and Break Bar. Through the CHITUBOX64 1.9.0 slicing software, the file is imported into the printer to start printing. Figure 2 shows a preparation flowchart of the vitrified bond diamond grinding wheel. After printing, the vitrified bond diamond grinding wheel was completed, and the excess resin was washed with alcohol and cured under ultraviolet light for 12 h.

**Figure 2.** Vitrified bond diamond grinding wheel preparation flowchart.**Table 3.** CAD model parameters.

	Outer Diameter/Length	Inner Diameter/Width	Thickness/Height
Grinding Wheel	100 mm	80 mm	10 mm
Flexural Bar	30 mm	6 mm	5 mm

To ensure a smooth process of photopolymerization printing, in addition to preparing a slurry with high solid content and low viscosity, it is necessary to set appropriate printing parameters. When ultraviolet light irradiates the slurry system composed of vitrified bonds and diamonds, the photopolymer resin absorbs the ultraviolet light. It undergoes a curing reaction while the glass particles reflect the ultraviolet light. The diamond particles with a darker color reduce the clarity of the ultraviolet light, weakening the radiation effect of light in the slurry and, thus, reducing the thickness of the cured layer. Numerous studies have shown that the influence of photopolymerization printing parameters on the fixed layer thickness follows Lambert–Beer’s law [34].

$$C_d = S_d \ln \left(\frac{E_0}{E_d} \right) \quad (1)$$

In Equation (1), E_0 represents the exposure energy formed on the surface of the slurry, E_d is the critical exposure energy of the slurry determined by the inherent properties of the material, S_d is the photosensitivity parameter, which is a function of particle properties and the optical properties of the photosensitive resin system, and C_d represents the cured layer thickness formed under the given exposure energy. By substituting the printer parameters into Equation (1), the range of E_0 values for the exposure energy is calculated, and the intensity of the light source is adjusted accordingly. The exposure time is controlled within the range of 2.0 to 2.5 s, during which the single-layer curing thickness of the slurry exceeds the layer thickness of 50 μm , satisfying the printing requirements.

2.5. Debinding and Sintering

Debinding and sintering are crucial parts of the experiment [35,36]. Improper debinding process will cause cracks, expansion, and other defects in the grinding wheel, which will lead to insufficient strength of the grinding wheel, and there will be dangerous behavior, such as cracking during high-speed grinding. Debinding in vacuum, the pyrolysis rate of organic matter is slow but it does not easily produce defects [37]. The oxygen content in the vacuum environment is scarce, and the carbon produced by the pyrolysis of organic matter cannot be removed by reaction. Therefore, we designed a two-step method to obtain a defect-free grinding wheel, first debinding in vacuum and then sintering in air. First, the organic matter is pyrolyzed in a vacuum environment, and then air is introduced to react the residual carbon with oxygen to eliminate impurities to the greatest extent.

2.6. Characterization

The particle size distribution of the vitrified bond with different milling times was analyzed using a laser particle size analyzer (M3001-XW-V00000, USA). The density of the vitrified bond was measured using a powder densimeter (SC-300, China) with 2.32 g/cm³. The rheological properties of different vitrified bond slurry systems were tested using a capillary rheometer (MLW-400, China). The stability of the vitrified bond slurries was measured through static sedimentation tests. Thermal analysis of the vitrified bond diamond grinding wheel green body was conducted using a thermogravimetric analyzer (DSC-200F3, Germany) with a heating rate of 10 °C/min to observe the combustion behavior of the photosensitive resin during heating. The physical phase analysis of the sintered grinding wheels was carried out using an X-ray diffractometer (D8 ADVANCE, Germany). The flexural strength of the sintered diamond grinding wheel specimens was measured using an electronic universal testing machine (WDW-50, China) with a span of 20 mm and a loading rate of 0.5 mm/min for the lower indenter, and five specimens were measured to take the average value. The density and porosity of the grinding wheel specimens were measured using the Archimedes drainage method. A scanning electron microscope (FEI INSPECT F50, USA) was used to observe the fracture micromorphology of the models. A Vickers microhardness tester (FM700, Japan) with a load of 50 kgf was used to measure the microhardness of the vitrified bond specimens. Five points were calculated to take the average value. The frictional wear of the grinding wheel grinding workpiece was tested

using a vertical universal friction and wear testing machine (MMW-1, China) with a load of 200 N, a rotational speed of 100 r/min, a grinding time of 500 s, and a grinding fluid of distilled water. The surface quality of the grinding wheel ground workpiece was observed using a white light interferometer (Zegege, USA).

3. Results and Discussion

3.1. Effects of Particle Size

Figure 3 shows the effect of different ball-milling times on the particle size of the vitrified bond. It was observed that as the milling time increased, the particle size gradually decreased. The d_{50} values of the vitrified bond were approximately 36.2 μm , 17.8 μm , 9.2 μm , and 4.8 μm for milling times of 1 h, 2 h, 4 h, and 6 h, respectively. It shows that prolonging the ball-milling time increases the number and energy of collisions between the balls and particles, which favors more particles breaking, thus reducing the particle size.

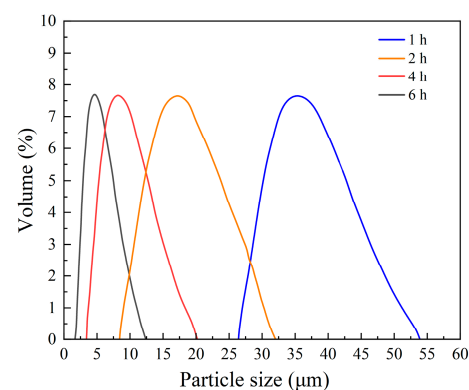


Figure 3. Particle size of vitrified bond with different ball-milling time.

The different particle sizes of the vitrified bond were mixed uniformly with the pre-prepared photosensitive mixture system (without dispersant) and ball-milled for 2 h to obtain the vitrified bond slurry. The effect of different particle sizes on the viscosity of the slurry was compared through rheological analysis, as shown in Figure 4. It was found that for vitrified bonds with d_{50} values of 36.2 μm , 17.8 μm , 9.2 μm , and 4.8 μm , the viscosities of the slurry at a shear rate of 30 s^{-1} were 1.42 Pa·s, 1.47 Pa·s, 1.50 Pa·s, and 1.54 Pa·s, respectively. This is because as the particle size decreases, the specific surface area of the particles increases, resulting in higher slurry viscosity. Combined with Figure 1, although the viscosity of the slurry system was lowest when the particle size d_{50} was 36.2 μm for 1 h of ball milling, some of the particles exceeded the thickness of the slicing layer by 50 μm , which might damage the equipment when printing, so a particle size d_{50} of 17.8 μm was selected for a ball-milling time of 2 h.

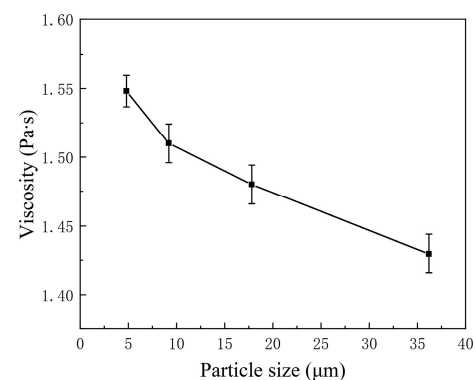


Figure 4. Viscosity of the slurries with different particle size.

3.2. Effects of Dispersant

Vitrified bond diamond wheels must possess sufficient strength to meet the demands of the grinding process, which requires a good dispersion of the bond and abrasive in the slurry. If the dispersibility is not good, there will be fewer raw materials and more resin in a particular area during the printing process, leading to defects during sintering. Therefore, to obtain a well-dispersed slurry, we investigated the effects of five dispersants on the viscosity of the slurry, taking into account existing research reports [27–29,36,38–40], and we set up a control group without any dispersant. The results are shown in Figure 5. It was found that PEG with a molecular weight of 200, OA, SA, SS, and SC (added at 5.0 wt.% relative to the powder weight) as dispersants, as well as the control group without dispersant, all exhibited shear-thinning behavior. This indicates that all five dispersants and the control group meet the minimum requirements for printing. At a shear rate of 30 s^{-1} , the viscosity of the slurry with the five dispersants was $0.48\text{ Pa}\cdot\text{s}$, $0.52\text{ Pa}\cdot\text{s}$, $0.92\text{ Pa}\cdot\text{s}$, $2.22\text{ Pa}\cdot\text{s}$, and $3.42\text{ Pa}\cdot\text{s}$, respectively, while the viscosity of the slurry without dispersant was $1.47\text{ Pa}\cdot\text{s}$. When PEG was used as a dispersant, the slurry exhibited the lowest viscosity, indicating its ability to effectively reduce particle collisions resulting from Brownian motion and minimize the friction between particles, thereby reducing the viscosity. On the other hand, SS and SC, when used as dispersants, have a viscosity beyond that of the slurry without dispersant, indicating their tendency to promote particle aggregation and collision without effectively reducing the slurry viscosity.

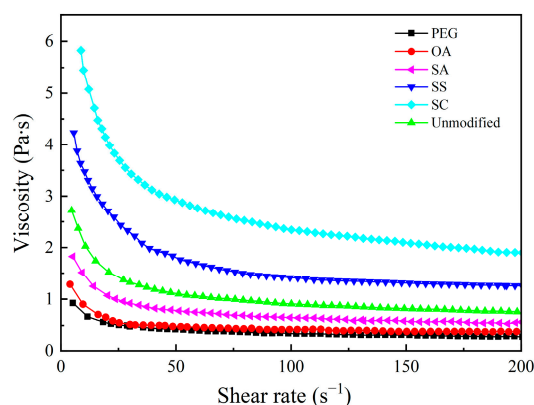


Figure 5. Viscosity of the slurries with different dispersants.

Considering the significant effect of PEG with a molecular weight of 200, OA, and SA in reducing the viscosity of the slurry, the influence of their addition at various concentrations on the slurry viscosity was compared. The concentrations tested were 1.0, 3.0, 5.0, and 7.0 wt.% (relative to the total weight of the powder), as illustrated in Figure 6. The research revealed that with an increase in the content of these three dispersants, the viscosity of the slurry showed a decreasing trend followed by an increasing trend; the minimum value of viscosity was obtained at an addition level of 5.0 wt.%. This indicates that when the concentration of the dispersant is too low, not all vitrified bond particles in the slurry are fully adsorbed by the dispersant, leading to ineffective modification. Due to the particle collisions resulting from Brownian motion, the particles not covered by the dispersant tend to agglomerate, resulting in poor dispersion and high viscosity. The dispersant forms a network structure within the slurry at an appropriate concentration. It creates an organic protective layer on the particle surfaces, preventing particle collisions and improving dispersion, thereby reducing viscosity—however, there are many free dispersant bridges and crosslinks between the particles at high dispersant concentrations. According to the DLVO theory [41], bridging can cause flocculation, increasing the internal friction of the slurry and reducing its stability, leading to an increase in viscosity. Therefore, PEG as a dispersant at a concentration of 5.0 wt.% is more suitable.

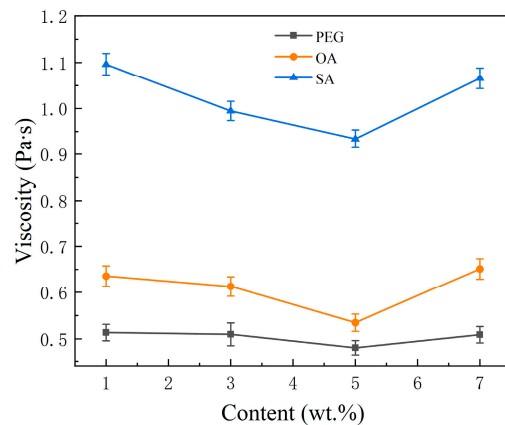


Figure 6. Viscosity of the slurries with different dispersant contents.

To determine the effect of molecular weight on the viscosity of the vitrified bond slurry, PEG with molecular weights of 200, 400, 800, 1000, and 2000 was investigated, as shown in Figure 7. The study revealed that as the molecular weight increased, the viscosity of the slurry also increased. At a shear rate of 30 s^{-1} , the viscosities were measured to be 0.48, 0.60, 1.26, and $2.07 \text{ Pa}\cdot\text{s}$ for PEG with molecular weights of 200, 400, 800, and 1000, respectively. This can be attributed to the fact that as the molecular weight of the dispersant increases, the molecules become longer and heavier, leading to a more complex spatial arrangement between the molecules. The intermolecular forces, such as van der Waals forces and electrostatic attraction, among these molecules increase the tendency of the dispersant molecules to aggregate within the slurry. This aggregation increases the intermolecular friction within the slurry, increasing viscosity. Therefore, PEG with a molecular weight of 200 is more suitable as a dispersant.

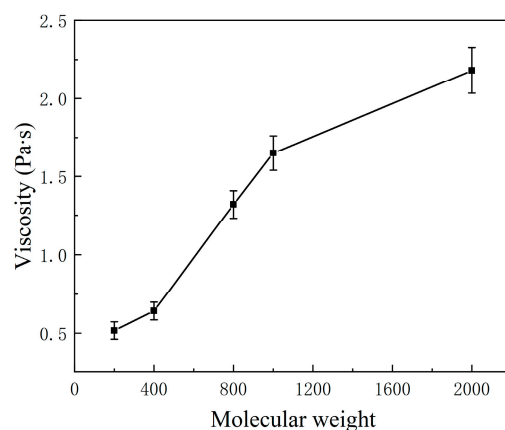


Figure 7. Viscosity of the slurries with different dispersant molecular weights.

The stability of vitrified bond slurry can be primarily measured through sedimentation tests. The prepared slurry is placed in a 10 mL graduated cylinder, and the height of the supernatant liquid (H_1) and the initial size of the slurry (H_0) are recorded every 12 h. The value of H_1/H_0 is then calculated, and a lower value of H_1/H_0 indicates higher slurry stability. To obtain a well-stabilized vitrified bond slurry, the effects of three dispersants that significantly reduced the viscosity of the slurry, PEG with a molecular weight of 200, OA, and SA (added at 5.0 wt.% relative to the total weight of the powders), were compared with the effects of a blank control group with no dispersant on the stability of the slurry, as shown in Figure 8. Figure 8a, 8b, 8c and 8d represent the sedimentation behavior of slurry samples with PEG, OA, SA, and no dispersant, respectively, after 120 h of sedimentation. At the same time, Figure 8e shows the H_1/H_0 values. This study revealed that after 120 h of

sedimentation, the supernatant liquid (H_1) heights for the four dispersants were 1.6, 3.7, 2.9, and 7.5 mL, respectively. As a dispersant, PEG exhibited the smallest H_1/H_0 value, which maintained the best stability of the slurry. This can be attributed to the excellent coverage of the PEG molecular chains on the surface of the vitrified bond particles, effectively reducing the contact and collision between the particles, resulting in slower sedimentation of the slurry. The slurry system without a dispersant showed the maximum height of the supernatant liquid in a short period, indicating severe aggregation and flocculation. This led to solid sedimentation and a faster sedimentation rate, making the slurry the least stable.

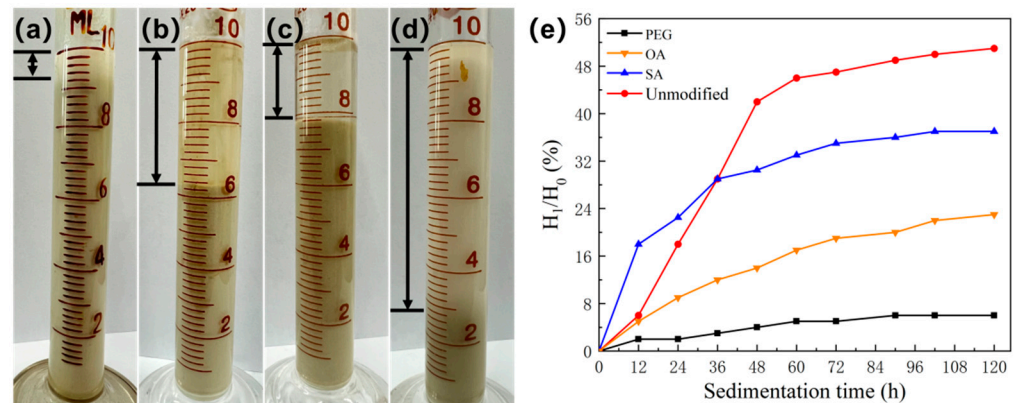


Figure 8. Stability of the slurry with different dispersants: (a) PEG; (b) OA; (c) SA; (d) unmodified; (e) H_1/H_0 value.

3.3. Effects of Solid Content

On the premise of guaranteeing the solid content of the vitrified bond slurry, lower viscosity is conducive to improving the slurry dispersion to meet LCD photopolymerization requirements. To meet the needs of the rheological properties of the slurry under the premise of raising the solid content, it helps to improve the printing accuracy. It is conducive to reducing the proportion of organic matter. In the later degreasing and sintering processes, it is conducive to avoiding defects such as cracking raw blanks and ensuring the densification of the wheel green body and grinding processing performance.

To obtain a vitrified bond slurry with high solid content and low viscosity, we investigated the rheological performance of the slurry with PEG of molecular weight 200 (added at 5.0 wt.% relative to the total weight of the powder) as a dispersant and different solid contents, as shown in Figure 9. Figure 9a illustrates the variation in slurry viscosity with shear rate. It was found that the slurry viscosity gradually decreased as the shear rate increased from 1 s^{-1} to 200 s^{-1} . This indicates that the slurry with different solid contents exhibits shear-thinning behavior and good dispersion. Many researchers have found this phenomenon [27,28]. Figure 9b is a scatter diagram of the viscosity of the slurry with different solid contents at a shear rate of 30 s^{-1} . The viscosity of the slurry is 0.48, 1.2, 1.65, 2.72, 3.82, and 6.53 Pa·s when the solid content is 40, 50, 55, 60, 65, and 70 wt.%. The red curve represents the Krieger–Dougherty model curve, which reflects the relationship between slurry viscosity and solid content [42]. As the solid content increases, the slurry viscosity increases significantly, and the trend of viscosity change aligns well with the model curve. The viscosity increase is most pronounced when the solid content increases from 65 wt.% to 70 wt.%, indicating that at higher substantial ranges, more severe clustering occurs within the slurry. This clustering, along with sedimentation effects, prevents the interlayer flow of the slurry even at high shear rates, resulting in a sharp increase in viscosity. Therefore, adding 5 wt.% PEG with a molecular weight of 200 and a solid content of 65 wt.% (approximately 45.5 vol.%) is most suitable. Compared with other research on the solid content of slurry, this experiment has made great progress [35,43].

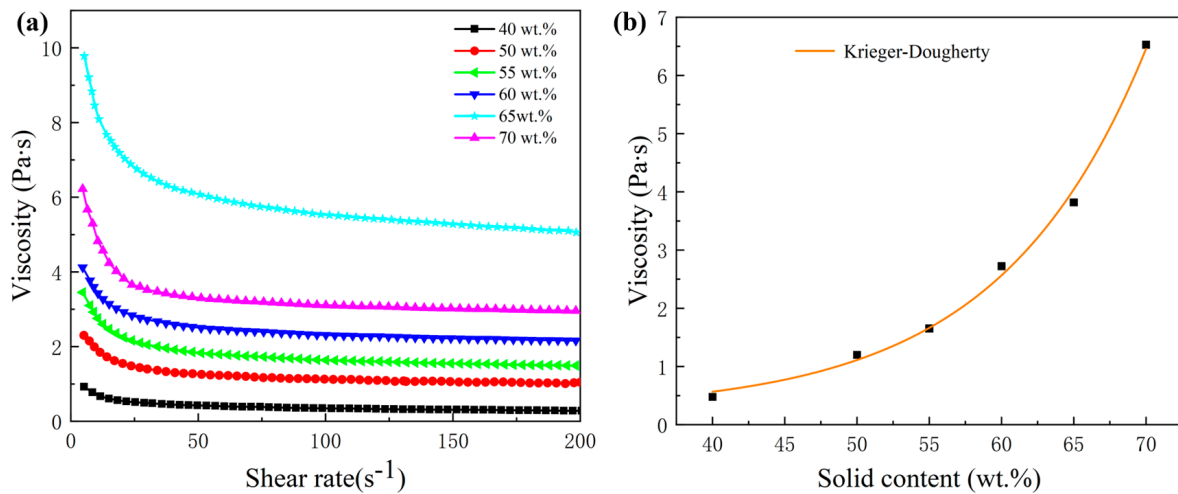


Figure 9. Viscosity at different solid contents (5 wt.% PEG of molecular weight 200): (a) relationship between shear rate and viscosity; (b) viscosity of slurry with different solid contents and Krieger–Dougherty model curves (30 s⁻¹).

3.4. Effects of Debinding and Sintering

After sintering, a two-step process was employed to obtain defect-free vitrified bond diamond grinding wheels. Firstly, debinding was performed in a vacuum environment to ensure the slow pyrolysis of organic materials and avoid generating defects. After debinding, oxygen was introduced for sintering in an ambient air environment to react with the residual carbon and eliminate impurities to the maximum extent. Previous studies have reported the pyrolysis temperatures of the photopolymer resins HDDA and TMPTA to be approximately 290 °C and 200 °C [35,43], while the pyrolysis temperature of PEG is about 300 °C. Based on the thermogravimetric analysis of the preforms (40 wt.% solids, 5.0 wt.% molecular weight 200 PEG), a slow debinding process was established, as shown in Figure 10. During the debinding stage, the temperature was held at 200, 300, 370, and 550 °C for 120 min at a rate of 1 °C/minute and 370–550 °C at a rate of 2 °C/minute. During the sintering stage, a heating rate of 2 °C/min was applied, followed by holding temperatures of 600 °C, 630 °C, 650 °C, 680 °C, and 700 °C for 150 min, as depicted in Figure 10b. After cooling to room temperature, defect-free vitrified bond diamond grinding wheels were obtained.

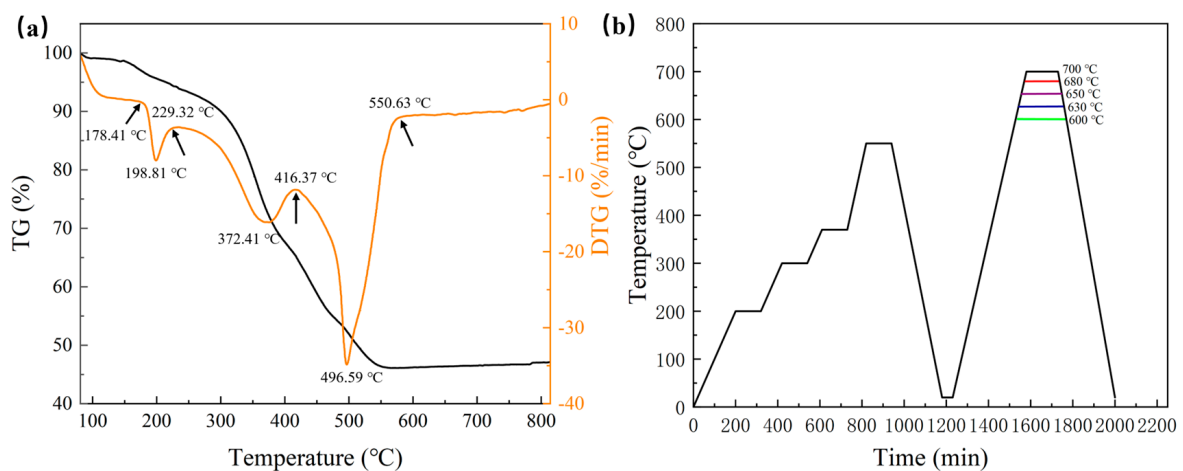


Figure 10. (a) Thermogravimetric analysis of green body; (b) two-step curve for sintering in air with debinding in vacuum.

The density, porosity, microhardness, and flexural strength of vitrified bond samples for different sintering temperatures are shown in Figure 11. Flexural strength, microhardness, and density were discovered to display a tendency of initially rising and subsequently decreasing with the rise in sintering temperature. The most significant values were attained at a sintering temperature of 680 °C, reaching 63.37 MPa, 807 MPa, and 2.24 g/cm³, respectively. At first, the porosity declined; then, it grew until it reached a minimum of 35.2% at 680 °C. The data are further explained by the microstructure of the vitrified bond samples at various sintering temperatures, as depicted in Figure 12. The pieces exhibited lower density and higher porosity below the optimal sintering temperature. This indicates a weaker occurrence of solid-state sintering reactions and weaker interactions among the bond components. This resulted in lower strength. When the sintering temperature exceeded the optimum, the liquid phase in the bond increased, leading to increased fluidity at high temperatures. The trapped pores inside the bond could not be expelled, resulting in over-sintering and foaming, leading to an increase in porosity and a decrease in strength. Therefore, a sintering temperature of 680 °C was more suitable. Due to the low solid content, the overall performance of the vitrified bond was relatively low. Using LCD photopolymerization technology, enhancing the solid content becomes a key factor for the future development of vitrified bond diamond grinding wheels.

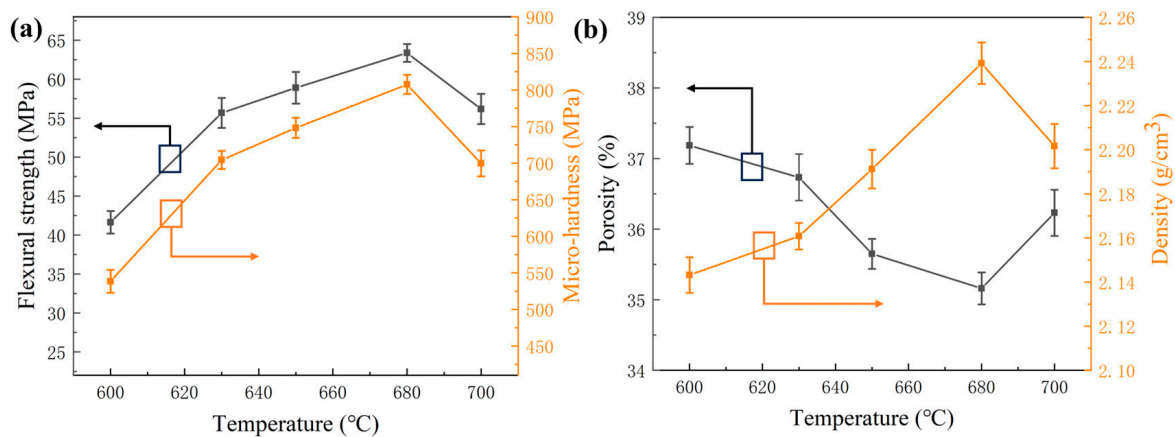


Figure 11. Vitrified bond at different sintering temperatures: (a) flexural strength and micro-hardness; (b) density and porosity.

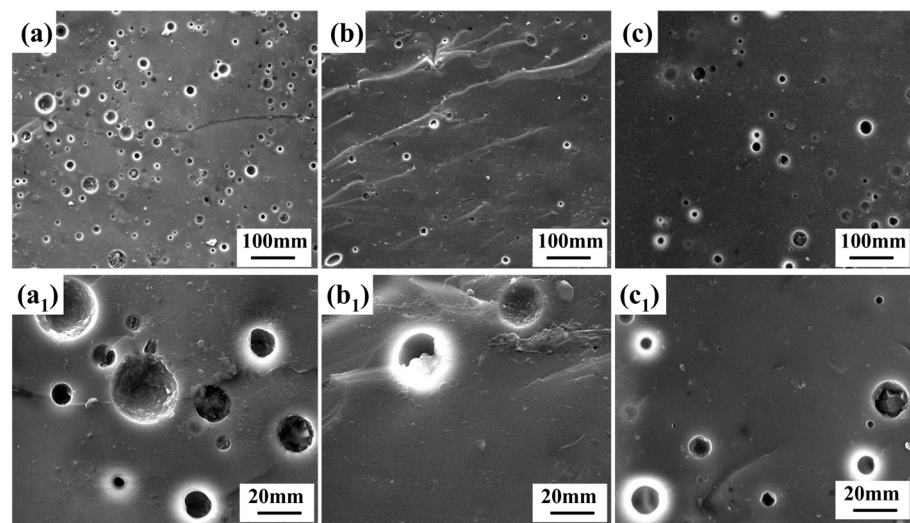


Figure 12. Microstructure at different sintering temperatures: (a,a₁) 630 °C; (b,b₁) 680 °C; (c,c₁) 700 °C.

3.5. Effects of Grit Ratio

The formulation of the grinding wheel is an essential feature of the wheel. The grit-to-bond ratio is the mass or volume ratio between the abrasive and the bond. The main abrasive is diamond in the vitrified bond diamond grinding wheels. Extensive experimental exploration was conducted to achieve sharp cutting edges for machining brittle materials and to meet printing requirements. It was found that when the diamond content exceeds 30 wt.%, it becomes difficult to shape the wheel due to reduced light transmission caused by the darker color of the diamond particles. Therefore, the content of the diamond is 30 wt.%, and the average particle size is 10 μm . White corundum (Al_2O_3) with an average particle size of 7 μm was selected as the auxiliary abrasive, which could improve the ratio of sand to bond, and trace white corundum could also increase the strength of the abrasive. To ensure the power of the grinding wheel after sintering, a higher content of vitrified bond is used in the formula of the grinding wheel. To investigate the influence of the grit-to-bond ratio on vitrified bond diamond grinding wheels, the formulated compositions are presented in Table 4. Using the above slurry formula, when the solid content of the slurry mixed with the vitrified bond and the abrasive is 65 wt.%, and the shear rate is 30 s^{-1} , the viscosity of the five groups of formulations is within $4.0\text{ Pa}\cdot\text{s}$, which can meet the printing requirements. With the decrease in white corundum content, the volume fraction of the solid drops. A slurry system composed of 42.8 vol.% vitrified bond and abrasive was successfully prepared.

Table 4. Formulation of vitrified bond diamond grinding wheels.

	Diamond	White Corundum	Vitrified Bond	Solid Content	Viscosity ($\text{Pa}\cdot\text{s}$)
R1	30 wt.%	20 wt.%	50 wt.%	65 wt.% (37.7 vol.%)	3.69
R2	30 wt.%	15 wt.%	55 wt.%	65 wt.% (38.6 vol.%)	3.78
R3	30 wt.%	10 wt.%	60 wt.%	65 wt.% (40.5 vol.%)	3.82
R4	30 wt.%	5 wt.%	65 wt.%	65 wt.% (41.9 vol.%)	3.89
R5	30 wt.%	0 wt.%	70 wt.%	65 wt.% (42.8 vol.%)	3.92

The wear resistance of grinding wheels directly reflects their durability; however, wear resistance is generally not directly measurable. Therefore, flexural strength is used as an indirect measure of the wear resistance of wheels. Figure 13 illustrates the flexural strength of grinding wheel samples with different grit-to-bond ratios at a sintering temperature of $680\text{ }^\circ\text{C}$. This study reveals that with an increase in the content of vitrified bond, the flexural strength of the grinding wheel samples initially increases and then decreases, reaching a maximum value of 46.78 MPa at a vitrified bond content of 30 wt.%. The flexural strength of the grinding wheel prepared by LCD photopolymerization is slightly higher than that prepared using the DIW method [19] but lower than that prepared using the traditional method [35,44,45]. This indicates that when the content of the vitrified bond is too low, the bonding force between the abrasive and the bond is insufficient, resulting in a lower flexural strength. Once the addition of vitrified bond reaches its peak, the excessive bond does not effectively infiltrate the abrasive, leading to foaming or even deformation between the cement and the abrasive, further reducing the strength. Solely relying on flexural strength is insufficient to test the grinding performance of grinding wheels; therefore, subsequent grinding experiments are necessary.

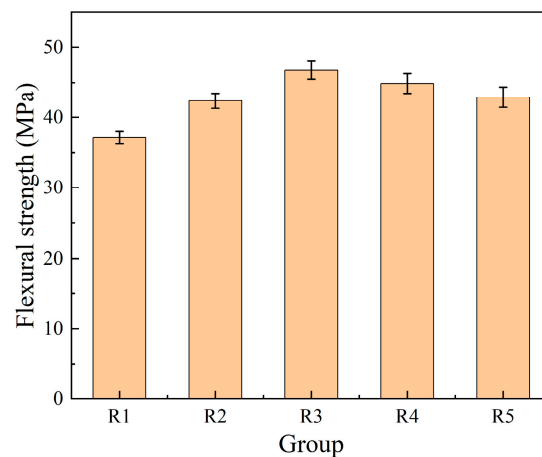


Figure 13. Flexural strength of different grit ratio at sintering temperature of 680 °C.

Figure 14 shows the X-ray diffraction pattern of the grinding wheel at a sintering temperature of 680 °C. This study reveals the presence of a glass phase in the phase composition of the grinding wheel, indicating the amorphous structure of the vitrified bond. The main component of white corundum is Al_2O_3 . In the spectrum, diamond and Al_2O_3 represent the grinding wheel's primary and auxiliary abrasive. The high-temperature sintering of diamond occurs without any occurrence of graphitization when adequately encapsulated by the vitrified bond.

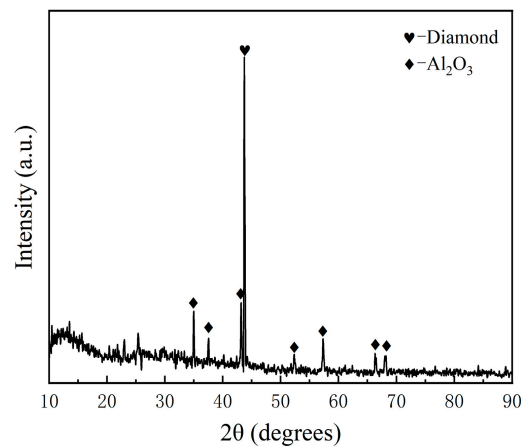


Figure 14. XRD pattern of sintered grinding wheel.

3.6. Grinding Experiment

Figure 15 presents a vitrified bond diamond grinding wheel prepared via LCD photopolymerization, Figure 15a is the top view of the grinding wheel, and Figure 15b is the side view of the grinding wheel. Table 5 shows the sintered shrinkage of the grinding wheels. Due to the lower solid content, the grinding wheels exhibit significant overall post-sintering shrinkage, with the maximum shrinkage observed in the thickness direction at 24.5%. This is attributed to the layer-by-layer stacking during the printing process. The grinding wheels with lower strength are prone to accidents when grinding, so four groups of wheels with four formulations, R2, R3, R4, and R5, which have higher flexural strength, were subjected to grinding experiments, compared, and analyzed, and then the optimal formulation was selected.

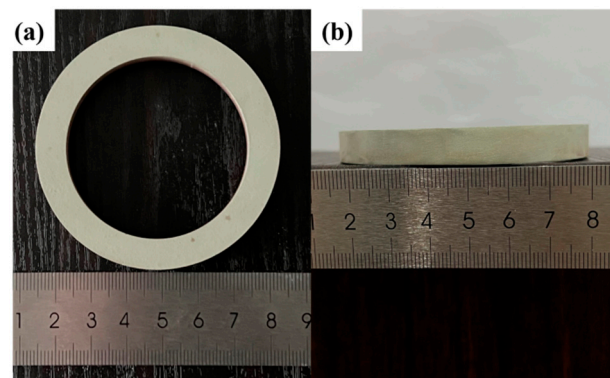


Figure 15. Vitrified bond diamond grinding wheel prepared by LCD photopolymerization.

Table 5. Grinding wheel sintering shrinkage.

	Outer Diameter	Inner Diameter	Thickness
pre-sintering	100 mm	80 mm	10 mm
post-sintering	77.60 mm	62.44 mm	7.55 mm
Shrinkage	22.40%	21.95%	24.5%

The grinding wheel was fixed on a customized substrate to grind silicon carbide ceramics in a vertical universal friction and wear testing machine. The grinding time was set to 500 s, and the friction and wear behavior of four different formulations of diamond wheels were tested. Table 6 presents the experimental data from the grinding tests. It was found that the material removal rate and grinding rate of the R3 wheel were a maximum of 5.08 mg/s and 9.78 among the four groups of wheels, respectively. This is because when the vitrified bond content is too low (less than 60 wt.%), the bond has a lower holding power on the abrasive, which causes more severe abrasive shedding when grinding, resulting in the most severe wheel loss and the smallest grinding ratio and material removal rate. On the other hand, when the vitrified bond content was too high (greater than 60 wt.%), the bonding force between the abrasive and the bond increased, making it difficult for the worn abrasives to detach from the wheel surface. As a result, the self-sharpening and sharpness of the wheel deteriorated. Although the wheel wear was reduced, the workpiece's material removal rate and grinding ratio decreased. Therefore, optimal grinding performance was achieved when the diamond content was 30 wt.%, the white corundum content was 10 wt.%, and the vitrified bond content was 60 wt.%, with a grit-to-bond ratio of 4:6 between the abrasive and the bond.

Table 6. Grinding data analysis.

	Wheel Wear (g)	Workpiece Removal (g)	Removal Rate (mg/s)	Grinding Ratio
R2	0.28	1.25	2.50	4.46
R3	0.26	2.54	5.08	9.78
R4	0.24	2.12	4.24	8.83
R5	0.22	1.45	2.90	6.59

Figure 16 shows the relationship between the friction coefficient and when four grinding wheels are used to grind the hard and brittle material silicon carbide ceramics. Deionized water was used as grinding fluid. The temperature of the workpiece surface during grinding is measured by a temperature measuring gun. The average temperature is 115 °C. It was found that the friction coefficient of the R2 wheel was stable at about 0.5 at the initial stage of grinding, and after 100 s, the friction coefficient increased, the fluctuation increased, and the stability was poor, which could be attributed to the low initial friction, and the bond could effectively maintain the diamond grains and maintain a stable

friction coefficient. This can be attributed to the low initial friction, allowing the glue to hold the diamond grits effectively and maintain a stable friction coefficient. However, as grinding time increased, the friction force also increased. Still, the limited bond failed to firmly retain the diamond grits, resulting in more unworn determinations falling off and causing more significant fluctuations in the friction coefficient. In contrast, the R3 grinding wheel maintained a stable friction coefficient of around 0.5 with minimal volatility. This stability can be attributed to its high strength, which allowed the diamond grits to quickly dislodge after becoming dull, ensuring a stable grinding process and excellent efficiency. The R4 grinding wheel gradually increased the friction coefficient from 0.3 to 0.6 as grinding time increased, followed by stability. This behavior occurred because, before 200 s of grinding, the sharp diamond grits produced more debris adhering to the grinding wheel and workpiece surfaces. Consequently, the spirits could not dislodge promptly, leading to an increase in the friction force and the friction coefficient. However, after 200 s of grinding, the friction force increased further, but the dulled diamond grits could then dislodge promptly, resulting in improved grinding process stability. Regarding the R5 grinding wheel, significant changes in the friction coefficient were observed after 120 s of grinding, with the most dramatic fluctuations occurring in the last 50 s. The excessive bond content led to slower dislodging of the diamond grits after wear, causing increased friction during workpiece grinding, resulting in more significant fluctuations in the friction coefficient and poorer grinding performance.

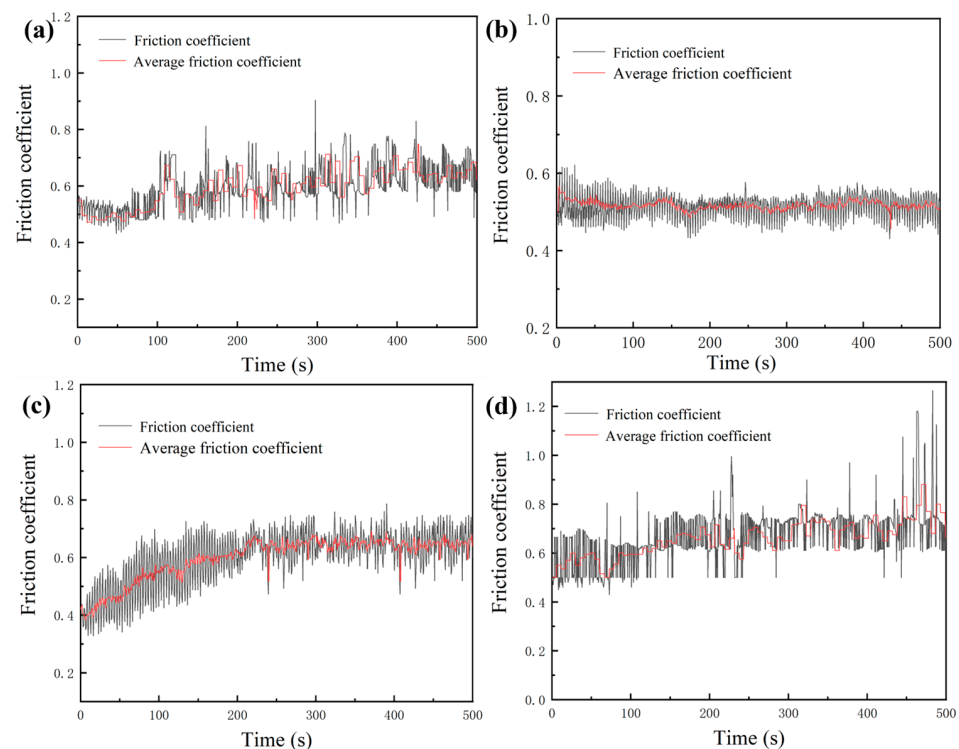


Figure 16. Relationship between friction coefficient and grinding time for grinding silicon carbide ceramics with four sets of grinding wheels: (a) R2; (b) R3; (c) R4; (d) R5.

The surface morphology of the silicon carbide workpieces after grinding with the four grinding wheels was examined using a white light interferometer, as shown in Figure 17. In the image, the red color represents surface protrusions, the blue color represents surface depressions, and the green color represents relatively flat areas. This study found that the average surface roughness S_a of the workpieces after grinding with the four sets of grinding wheels was $2.144\ \mu\text{m}$, $1.767\ \mu\text{m}$, $2.047\ \mu\text{m}$, and $2.284\ \mu\text{m}$, respectively. The surface roughness depends mainly on the abrasive grain size. The surface roughness difference was insignificant since the diamond particle size used in the four sets of grinding wheels

was the same. However, a detailed analysis revealed that the R3 grinding wheel exhibited the lowest surface roughness and the best surface flatness. It had fewer depressions and protrusions. This can be attributed to the higher flexural strength and sharper cutting edges of the wheel, resulting in better self-sharpening. When grinding hard and brittle materials, a shorter wheel tends to produce lower surface roughness on the workpiece. From the grinding experiment, the grinding performance of the grinding wheel meets the daily processing.

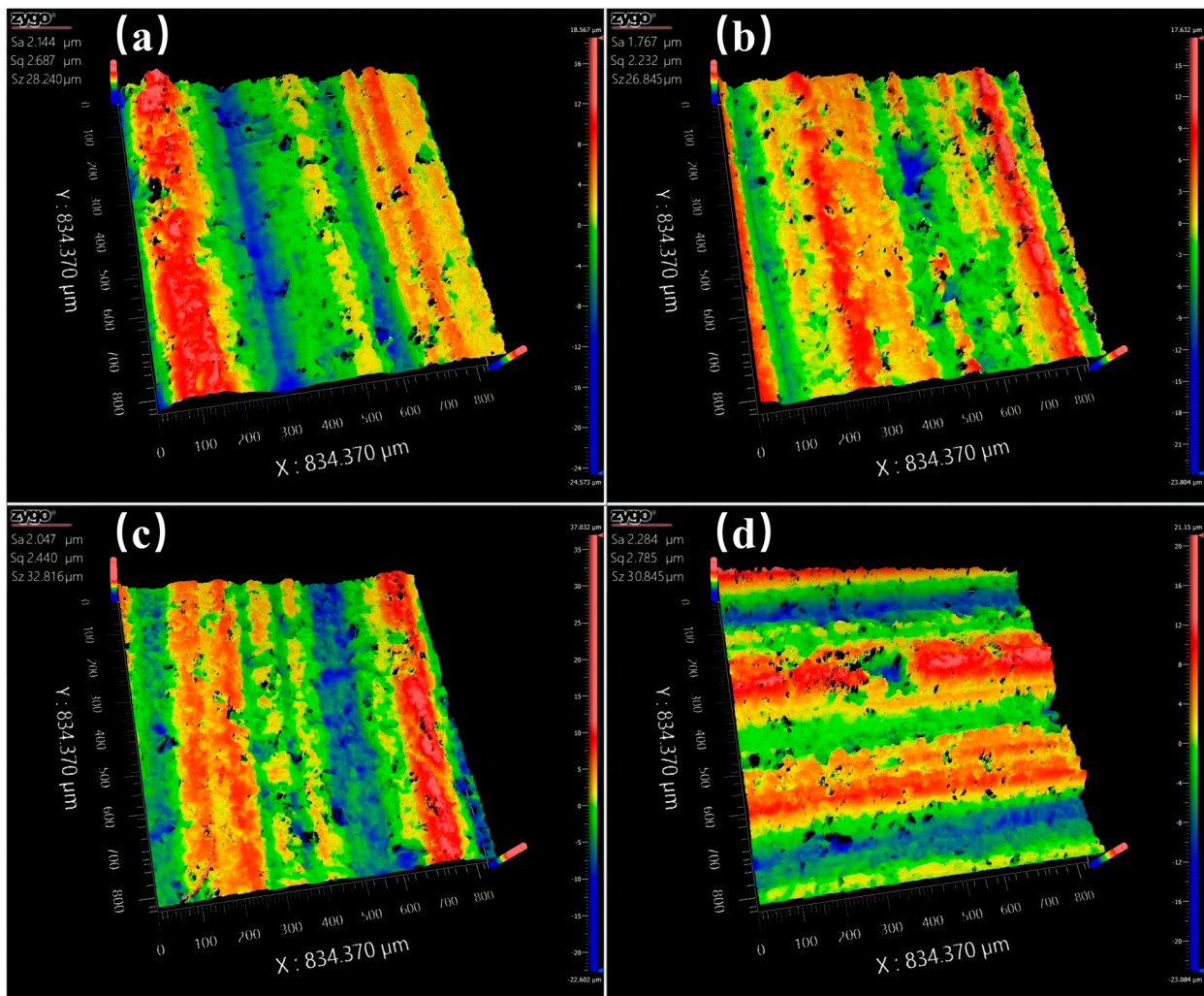


Figure 17. Surface quality analysis of silicon carbide grinding with 4 sets of vitrified bond diamond grinding wheels: (a) R2; (b) R3; (c) R4; (d) R5.

4. Conclusions

This study proposes a successful method for fabricating vitrified bond diamond grinding wheels via LCD photopolymerization 3D printing, utilizing high-temperature melting ceramic raw materials as vitrified bonds. The following conclusions are drawn:

- (1) The utilization of PEG with a molecular weight of 200 at a dosage of 5.0 wt.% (relative to the total weight of the powder) as a dispersant yielded the highest dispersion and stability of the vitrified bond slurry, accompanied by the lowest viscosity. Successful fabrication was achieved with a maximum solid content of 65 wt.% (approximately 45.5 vol.%) in the slurry, meeting the requirements for printing.
- (2) A two-step debinding and sintering method was proposed for vitrified bond green bodies, in which the specimens can be sintered in the air after slow debinding in a vacuum environment, and samples without defects can be obtained. The flexural

strength, microhardness, and density of the model at a sintering temperature of 680 °C were maximized to 63.37 MPa, 807 MPa, and 2.24 g/cm³, respectively, and the porosity was minimized to 35.2% at this temperature.

- (3) Five grinding wheel formulations with different grit-to-bond ratios were studied. Vitrified bond and abrasive slurry systems with a solid content of 65 wt.% (approximately 42.8 vol.%) were prepared. When the diamond content is 30 wt.%, white corundum content is 10 wt.%, and vitrified bond content is 60 wt.%, i.e., when the grit-to-bond ratio is 4:6, the flexural strength, material removal rate, and grinding balance of the grinding wheels are all maximal at 46.78 MPa, 5.08 mg/s, and 9.78, respectively. The coefficient of friction is stable at about 0.5 during grinding.
- (4) In the experiment of grinding hard and brittle material silicon carbide, the surface roughness of workpieces honed by four groups of diamond grinding wheels with more considerable flexural strength did not differ much. The surface roughness of the grinding wheels with vitrified bond content of 60 wt.% was the lowest at 1.767 μm, and the surface flatness was the best, with fewer depressions and raised parts.

Author Contributions: Conceptualization, Z.C.; methodology, P.H.; investigation, N.X. and Z.C.; writing—original draft, Z.C., G.B. and Z.W.; writing—review and editing, Z.C. and P.H.; funding acquisition, P.H. All authors have read and agreed to the published version of the manuscript.

Funding: This work is funded by the National Natural Science Foundation of China (No. 51802290), the Science and Technology Innovation Talents in Universities of Henan Province (Nos. 212102210463, 182102210613), and the Henan University of Technology High-level Talent Fund (No. 31400301).

Institutional Review Board Statement: Not applicable.

Informed Consent Statement: Not applicable.

Data Availability Statement: Data are contained within the article.

Conflicts of Interest: Author Zhao Wang was employed by the company Beijing Gangyan Diamond Products Company. The remaining authors declare that the research was conducted in the absence of any commercial or financial relationships that could be construed as a potential conflict of interest.

References

1. Dai, C.W.; Ding, W.F.; Zhu, Y.J.; Xu, J.H.; Yu, H.W. Grinding temperature and power consumption in high speed grinding of Inconel 718 nickel-based superalloy with a vitrified CBN wheel. *Precis. Eng.* **2018**, *52*, 192–200. [[CrossRef](#)]
2. Zhou, H.; Guo, M.; Wang, X. Ultraprecision grinding of silicon wafers using a newly developed diamond wheel. *Mat. Sci. Semicon. Proc.* **2018**, *68*, 238–244. [[CrossRef](#)]
3. Rabiey, M.; Jochum, N.; Kuster, F. High performance grinding of zirconium oxide (ZrO₂) using hybrid bond diamond tools. *CIRP Ann.* **2017**, *62*, 343–346. [[CrossRef](#)]
4. Liu, J.H.; Pei, Z.J.; Fisher, G.R. Grinding wheels for manufacturing of silicon wafers: A literature review. *Int. J. Refract. Met. Hard Mater.* **2017**, *47*, 1–13. [[CrossRef](#)]
5. Zhang, X.H.; Wang, Y.H.; Zang, J.B.; Cheng, X.Z. Improving oxidation resistance of diamond by adding silicon into diamond–borosilicate glass composites. *Int. J. Refract. Met. Hard Mater.* **2017**, *29*, 495–498. [[CrossRef](#)]
6. Xie, D.; Gan, X.P.; Xiong, H.W.; Li, Z.Y.; Zhou, K.C. Nano TiC modified Ti (C, N)-based cermets with weakened rim-binder interfaces. *Mater. Sci. Eng.* **2022**, *845*, 143194. [[CrossRef](#)]
7. Sun, J.L.; Chen, Y.; Zhao, J. Nano-ceramic replacing cobalt in cemented carbide as binder phase: Is it feasible? *J. Alloys Compd.* **2022**, *896*, 162968. [[CrossRef](#)]
8. Xia, P.; Jiang, R.G.; Li, Z.H.; Zhu, Y.M.; Zhai, C.X.; Feng, D.D.; Sun, P.H. Effect of Y₂O₃ on the properties of vitrified bond and vitrified diamond composites. *Compos. Part B-Eng.* **2022**, *67*, 515–520. [[CrossRef](#)]
9. Han, J.; He, F.; Wang, L.L.; Zhang, L.X.; Ye, C.Q.; Xie, J.L.; Mei, S.X.; Jin, M.F. Effect of WO₃ on the structure and properties of low sintering temperature and high strength vitrified bond. *J. Alloys Compd.* **2016**, *679*, 54–58. [[CrossRef](#)]
10. Li, Q.; Li, Z.H.; Feng, D.D.; Yang, T.; Li, Y. Comparison of rare earth oxides on properties of vitrified diamond composites. *Diam. Relat. Mater.* **2016**, *71*, 85–89. [[CrossRef](#)]
11. Karabulut, M.; Yuce, B.; Bozdogan, O.; Ertap, H.; Mammadov, G.M. Effect of boron addition on the structure and properties of iron phosphate glasses. *J. Non-Cryst. Solids* **2011**, *357*, 1455–1462. [[CrossRef](#)]
12. Yin, Y.H.; Xu, P.F.; Fang, J.B.; Yang, J.L. Effect of fly ash cenosphere@ SiO₂ core-shell microspheres on physical properties and microstructures of vitrified bond diamond tools. *Diam. Relat. Mater.* **2020**, *103*, 107703. [[CrossRef](#)]

13. Miao, W.P.; Ding, Y.L.; Zhao, Y.J.; Bao, H.; Yan, N.; Yang, W.; Hui, Z.; Liu, B. Modified gel casting technique to fabricate honeycomb structured vitrified-bonded ultrafine diamond grinding wheels. *Ceram. Int.* **2020**, *46*, 4462–4469. [[CrossRef](#)]
14. Upcraft, S.; Fletcher, R. The rapid prototyping technologies. *Assembly. Autom.* **2003**, *23*, 318–330. [[CrossRef](#)]
15. Chen, Z.W.; Li, Z.Y.; Li, J.J.; Liu, C.B.; Lao, C.S.; Fu, Y.L.; Liu, C.Y.; Li, Y.; Wang, P.; He, Y. 3D printing of ceramics: A review. *J. Am. Ceram. Soc.* **2019**, *39*, 661–687. [[CrossRef](#)]
16. Yang, Z.B.; Zhang, M.J.; Zhang, Z.; Liu, A.J.; Yang, R.Y.; Liu, S.A. A study on diamond grinding wheels with regular grain distribution using additive manufacturing (AM) technology. *Mater. Des.* **2016**, *104*, 292–297. [[CrossRef](#)]
17. Li, X.K.; Wang, C.; Tian, C.C.; Fu, S.L.; Rong, Y.M. Digital design and performance evaluation of porous metal-bonded grinding wheels based on minimal surface and 3D printing. *Mater. Des.* **2021**, *203*, 109556. [[CrossRef](#)]
18. Tian, C.C.; Li, X.K.; Zhang, S.B.; Guo, G.Q.; Ziegler, S.; Henrich, J.; Schleifenbaum; Wang, L.P.; Rong, Y.M. Porous structure design and fabrication of metal-bonded diamond grinding wheel based on selective laser melting (SLM). *Int. J. Adv. Manuf. Technol.* **2019**, *100*, 1451–1462. [[CrossRef](#)]
19. Huang, J.L.; Lu, J.; Wang, Y.H.; Ma, Z.Q. Fabrication of porous structure vitrified bond diamond grinding wheel via direct ink writing. *Ceram. Int.* **2021**, *47*, 34050–34058. [[CrossRef](#)]
20. Guo, L.; Zhang, X.R.; Chen, S.B.; Hui, J.Z. An experimental study on the precision abrasive machining process of hard and brittle materials with ultraviolet-resin bond diamond abrasive tools. *Materials* **2019**, *12*, 125. [[CrossRef](#)]
21. Guo, L.; Zhang, X.R.; Lee, C.H.; Marinescu, I.D.; Zhang, Y.H.; Hui, J.Z. An experimental study on the abrasive machining process of electronic substrate material with a novel ultraviolet-curable resin bond diamond lapping plate. *IEEE Access* **2019**, *7*, 64375–64385. [[CrossRef](#)]
22. Lin, T.; Liu, S.W.; Ji, Z.H.; Shao, H.P.; Hao, J.J. Vitrified bond diamond grinding wheel prepared by gel-casting with 3D printing molds. *Diam. Relat. Mater.* **2020**, *108*, 107917. [[CrossRef](#)]
23. Singh, S.; Ramakrishna, S.; Singh, R. Material issues in additive manufacturing: A review. *J. Manuf. Process.* **2017**, *25*, 185–200. [[CrossRef](#)]
24. Shahrubudin, N.; Lee, T.C.; Ramlan, R. An overview on 3D printing technology: Technological, materials, and applications. *Procedia Manuf.* **2019**, *35*, 1286–1296. [[CrossRef](#)]
25. Griffith, M.L.; Halloran, J.W. Freeform fabrication of ceramics via stereolithography. *J. Am. Ceram. Soc.* **1996**, *79*, 2601–2608. [[CrossRef](#)]
26. Griffith, M.L.; Halloran, J.W. Scattering of ultraviolet radiation in turbid suspensions. *J. Appl. Phys.* **1997**, *81*, 2538–2546. [[CrossRef](#)]
27. Adake, C.V.; Bhargava, P.; Gandhi, P. Effect of surfactant on dispersion of alumina in photopolymerizable monomers and their UV curing behavior for microstereolithography. *Ceram. Int.* **2015**, *41*, 5301–5308. [[CrossRef](#)]
28. Zhang, S.; Sha, N.; Zhao, Z. Surface modification of α -Al₂O₃ with dicarboxylic acids for the preparation of UV-curable ceramic suspensions. *J. Eur. Ceram. Soc.* **2017**, *37*, 1607–1616. [[CrossRef](#)]
29. Quan, H.Y.; Zhang, T.; Xu, H.; Luo, S.; Nie, J.; Zhu, X.Q. Photo-curing 3D printing technique and its challenges. *Bioact. Mater.* **2020**, *5*, 110–115. [[CrossRef](#)]
30. Shan, Y.J.; Krishnakumar, A.; Qin, Z.H.; Mao, H.C. Reducing lateral stair-stepping defects in liquid crystal display-based vat photopolymerization by defocusing the image pattern. *Addit. Manuf.* **2022**, *52*, 102653. [[CrossRef](#)]
31. Caplins, B.W.; Higgins, C.I.; Kolibaba, T.J.; Arp, U.; Miller, C.C.; Poster, D.L.; Zarobila, C.J.; Zong, Y.Q.; Killgore, J.P. Characterizing light engine uniformity and its influence on liquid crystal display based vat photopolymerization printing. *Addit. Manuf.* **2023**, *62*, 103381. [[CrossRef](#)]
32. Roohani, I.; Entezari, A.; Zreiqat, H. Liquid crystal display technique (LCD) for high resolution 3D printing of triply periodic minimal surface lattices bioceramics. *Addit. Manuf.* **2023**, *74*, 103720. [[CrossRef](#)]
33. Ding, G.J.; He, R.J.; Zhang, K.Q.; Xia, M.; Feng, C.W.; Fang, D.N. Dispersion and stability of SiC ceramic slurry for stereolithography. *Ceram. Int.* **2020**, *46*, 4720–4729. [[CrossRef](#)]
34. Mäntele, W.; Deniz, E. UV–VIS absorption spectroscopy: Lambert-Beer reloaded. *Spectrochim. Acta Part A Mol. Biomol. Spectrosc.* **2020**, *173*, 965–968. [[CrossRef](#)]
35. Liu, Y.; Zhan, L.A.; He, Y.; Zhang, J.; Hu, J.J.; Cheng, L.J.; Wu, Q.M. Stereolithographical fabrication of dense Si₃N₄ ceramics by slurry optimization and pressure sintering. *Ceram. Int.* **2020**, *46*, 2063–2071. [[CrossRef](#)]
36. He, R.J.; Ding, G.J.; Zhang, K.Q.; Li, Y.; Feng, D.N. Fabrication of SiC ceramic architectures using stereolithography combined with precursor infiltration and pyrolysis. *Ceram. Int.* **2019**, *45*, 14006–14014. [[CrossRef](#)]
37. Xu, X.B.; Li, P.Y.; Ge, C.H.; Han, W.F.; Zhao, D.; Zhang, X.D. 3D Printing of Complex-type SiOC Ceramics Derived From Liquid Photosensitive Resin. *ChemistrySelect* **2019**, *4*, 6862–6869. [[CrossRef](#)]
38. Lee, Y.H.; Lee, B.J.; Maeng, W.Y.; Koh, Y.H.; Kim, H.E. Photocurable ceramic slurry using solid camphor as novel diluent for conventional digital light processing (DLP) process. *J. Eur. Ceram. Soc.* **2019**, *39*, 4358–4365. [[CrossRef](#)]
39. Ding, G.J.; He, R.J.; Zhang, K.Q.; Xie, C.; Wang, M.; Yang, Y.Z.; Fang, D.N. Stereolithography-based additive manufacturing of gray-colored SiC ceramic green body. *J. Am. Ceram. Soc.* **2019**, *102*, 7198–7209. [[CrossRef](#)]
40. Jin, J.; Yong, Y.; Plabc, L.; Chen, J.M. Fine lattice structural titanium dioxide ceramic produced by DLP 3D printing. *Ceram. Int.* **2019**, *45*, 23007–23012.
41. Trefalt, G.; Borkovec, M. *Overview of DLVO Theory*; Laboratory of Colloid and Surface Chemistry, University of Geneva: Geneva, Switzerland, 2014; Volume 304.

42. Krieger, I.M.; Dougherty, T.J. A mechanism for non-Newtonian flow in suspensions of rigid spheres. *J. Rheol.* **1959**, *3*, 137–152. [[CrossRef](#)]
43. Zhang, K.Q.; He, R.J.; Ding, G.J.; Feng, C.W.; Song, W.D.; Fang, D.N. Digital light processing of 3Y-TZP strengthened ZrO₂ ceramics. *Mater. Sci. Eng.* **2020**, *774*, 138768. [[CrossRef](#)]
44. Li, K.; Zhao, Z. The effect of the surfactants on the formulation of UV-curable SLA alumina suspension. *Ceram. Int.* **2017**, *43*, 4761–4767. [[CrossRef](#)]
45. Chen, S.; Liu, X.; Wan, L. Effect of V₂O₅ addition on the wettability of vitrified bond to diamond abrasive and grinding performance of diamond wheels. *Diam. Relat. Mater.* **2020**, *102*, 107672. [[CrossRef](#)]

Disclaimer/Publisher's Note: The statements, opinions and data contained in all publications are solely those of the individual author(s) and contributor(s) and not of MDPI and/or the editor(s). MDPI and/or the editor(s) disclaim responsibility for any injury to people or property resulting from any ideas, methods, instructions or products referred to in the content.